Modeling of the Effect of Temperature, Frequency, and Phase Transformations on the Viscoelastic Properties of AA 7075-T6 and AA 2024-T3 Aluminum Alloys

JOSE I. ROJAS and DANIEL CRESPO

The viscoelastic response of commercial aluminum alloys 7075-T6 and 2024-T3 as a function of temperature is presented. Experimental data are obtained with a dynamic-mechanical analyzer (DMA) at different loading frequencies and compared with the available transmission electron microscopy (TEM) and differential scanning calorimetry (DSC) data. The effect of successive microstructural transformations (particle precipitation and redissolution) is revealed. An analytical model is developed, which fits the mechanical response up to 573 K (300 °C). The model takes into account the concentration of Guinier-Preston Zones (GPZ) and metastable precipitates (η' in AA 7075-T6 and θ'/S' in AA 2024-T3), allowing us to determine the kinetic parameters of these transformations. The activation energies were previously obtained by several authors from DSC measurements and other techniques, showing considerable dispersion. The presented data, obtained with a completely different technique, allow us to reduce the uncertainty on these data and show the potential of DMA measurements in the study of microstructural transformations.

DOI: 10.1007/s11661-012-1281-7

I. INTRODUCTION

MUCH research has been devoted to the characterization of most of the mechanical properties of materials. However, the viscoelastic behavior of metals, consequence of internal friction, has received much less attention. The comprehension of the underlying physics of this phenomenon is of high interest as structural materials are submitted to dynamic loads in most applications. Indeed, fatigue is the consequence of microstructural changes induced in a material under repeated loading, and the viscoelastic behavior is intimately linked to the microstructure.[1] This fact has been shown in metallic glasses, where structural relaxations, the glass transition, and the crystallization processes have been analyzed by dynamic-mechanical analysis.[2] Accordingly, the characterization of the viscoelastic response of a material offers an alternative method for analyzing its microstructure and fatigue behavior. In addition, it enables a deeper understanding of other technologically essential properties, like mechanical damping and yielding.[1]

The research reported in this article is aimed at the identification, characterization and modeling, whenever possible, of the effects of temperature, frequency of dynamic loading, and microstructure and phase transformations on the viscoelastic behavior of aluminum alloys (AA) 7075 and AA 2024. These alloys are key representatives of their respective families (*i.e.*, AlZnMg and AlCuMg alloys) that, after proper age-hardening processes, feature excellent mechanical properties[3] and are highly suitable to a number of industrial applications, especially in the aerospace sector and transport industry. For instance, these alloys are widely used in aircraft skin panels, especially in military aircraft[4–6] but also in commercial civil aviation aircrafts.[7]

Age hardening is based on the formation of intermetallic products from the decomposition of a metastable super-saturated solid solution (SSS), which is obtained by solution treatment and quenching. The interaction between the decomposition products and the dislocations is the main responsible for the hardening.[3] That is, the particular precipitation path and phase transformations, which in turn depend on the alloy composition, quenching conditions, and aging parameters,[8] determine the microstructure, and hence the material properties as well. This is the reason why appreciable research efforts have been focused on the investigation of the transformation sequence during aging in metals. This research has been particularly intense in AlZnMg alloys (series 7000)[9] and in AlCuMg alloys (series 2000) because of their commercial and industrial importance, for the reasons explained above.

For the alloys of the family AlZnMg, it is accepted that the age-hardening mechanism is based essentially on the following aging sequence[8–11]:

- α_{SSS} – GPZ I – GPZ II – η' – η

where GPZ are Zn/Mg solute-rich coherent clusters named Guinier-Preston Zones, η' the semicoherent (metastable) hexagonal $MgZn_2$ phase, and η is the incoherent stable (equilibrium) hexagonal $MgZn_2$ phase.

JOSE I. ROJAS, Teaching Assistant, and DANIEL CRESPO, Professor, are with the Escola d'Enginyeria de Telecomunicació i Aeroespacial de Castelldefels (EETAC), Universitat Politècnica de Catalunya (UPC Barcelona Tech), 08860 Castelldefels (Barcelona), Spain. Contact e-mail: josep.ignasi.rojas@upc.edu
Manuscript submitted May 24, 2011.

Published online: 18 July 2012

For the alloys of the family AlCuMg, it is widely accepted that the age-hardening mechanism is based on two different aging sequences, which depend on the Cu:Mg ratio[3,12–16]:

- α_{SSS} – GPZ I – GPZ II (θ'') – θ' – θ
- α_{SSS} – GPBZ – (S″) – S′ – S

where GPZ are Cu solute-rich coherent clusters named the Guinier-Preston Zones, θ'' and θ' are the semicoherent (metastable) Al_2Cu phases, θ the incoherent stable (equilibrium) Al_2Cu phase, GPBZ the Cu/Mg coherent clusters named Guinier-Preston-Bagariastkij zones, S″ and S′ are the semicoherent (metastable) Al_2CuMg phases, and S is the incoherent stable (equilibrium) Al_2CuMg phase.[3] The existence of an intermediate phase S″ between GPBZ and S′ is still a controversial issue, however. The AA 2024-T3 used in this research contains 4.46 wt pct Cu and 1.35 wt pct Mg. In view of the AlCuMg phase diagram, this alloy should age according to both precipitation paths, leading finally to formation of both θ and S phases, which indeed has been confirmed by electron microscopy.[14]

Finally, in the case of AlZnMgCu alloys, apart from the latter precipitation sequences, that of AlZnMg is present as well. There are no indications of possible interactions between these three different sequences, which seem to develop independently.[13]

A. *Modeling of Phase Transformation Kinetics of AlZnMg and AlCuMg Alloys*

In phase transformations, thermodynamic effects, kinetic effects, and mass transport usually appear interrelated.[17] Significant research has been devoted to the study and modeling of these effects in the phase transformations that characterize the precipitation sequences of the AlZnMg and AlCuMg families. In particular, several types of rate equations have been proposed also that establish the time-evolution of the transformed fraction* during the corresponding transformation. For instance, the Johnson–Mehl–Avrami–Kolmogorov (JMAK) model is commonly is commonly used to describe the kinetics of nucleation and growth transformations, where the formation of a new phase typically follows a sigmoidal curve.[17–19] This equation can be stated as

$$Y(t) = 1 - \exp(-(t/\tau)^n) \qquad [1]$$

where Y is the transformed fraction, t is time, τ is the characteristic transformation time, and n is the Avrami exponent. The transformation time is determined by the activation energy and the transformation temperature, and thus, it will decrease as the transformation temperature increases. The Avrami exponent depends on the nature of the nucleation (continuous or site saturated) and growth (two-dimensional [2-D] or three-dimensional [3-D], interface, or diffusion-controlled) processes.[18] It is noteworthy that the Avrami model relates only to kinetics and stems simply from geometrical considerations (*i.e.*, the rate of occupation of the space by the new phase), and its application does not require any assumption or consideration regarding the thermodynamics of the transformation.

From differential isothermal calorimetry (DIC) scans, Smith[12] obtained information on the kinetics of phase transformations of AA 2124 using a two-exponential fit and a rate-averaged time constant. However, GPZ formation was best fitted to a JMAK kinetics model.[12] Papazian[20] studied the GPZ dissolution processes for AA 2219 and AA 7075. Experimental differential scanning calorimetry (DSC) data were fitted to a 3-D volume diffusion limited rate expression (Eq. [2]) and a first-order diffusion expression (Eq. [3]):

$$\left[1 - (1 - Y)^{1/3}\right]^2 = \frac{k_0 E_A}{K\phi} \int_{\frac{E_A}{KT}}^{\infty} \frac{e^{-x}}{x^2} dx \qquad [2]$$

$$-\ln(1 - Y) = \frac{k_0 E_A}{K\phi} \int_{\frac{E_A}{KT}}^{\infty} \frac{e^{-x}}{x^2} dx \qquad [3]$$

where k_0 is a preexponential coefficient, E_A is the activation energy (assumed to be constant), K is the Boltzmann constant, Φ is the DSC heating rate, and T is temperature. For AA 2219 aged at a low temperature, Papazian concluded that GPZ dissolution is best described by the 3-D volume diffusion limited rate expression (Eq. [2]). For AA 7075 aged at a low temperature, *i.e.*, aged 6 months at room temperature (RT), and AA 7075-T651, Papazian concluded that the GPZ dissolution in AA 7075 is best described also by the 3-D volume diffusion limited rate expression (Eq. [2]).

The rate of formation of θ' is best described by an Avrami expression with $n = 1.1$.[20] S′ formation has also been modeled using the Avrami equation with $n = 1.0$.[14] For η' phase formation and growth in as-quenched specimens and aged specimens, the Avrami index has been inferred to be about 2.3 to 2.8 (±20 pct).[21]

Alternative expressions for modeling the transformation kinetics are also reported in the literature. For instance, assuming that the particular phase transformation is a temperature- or thermally-activated process, the concentration of the species may follow the Arrhenius behavior. In this case, the transformation rate equation is[15,18]

$$\frac{dY}{dt} = f(Y) k_0 \exp\left(-\frac{E_A}{KT}\right) \qquad [4]$$

Jena *et al.*[15] stated that precipitation reactions that occur by nucleation and growth yield sigmoidal behavior and are best described either by the Avrami model in Eq. [1], or by Eq. [4] when

*The dimensionless transformed fraction or simply transformed fraction is the ratio concentration-to-initial concentration in dissolution processes and the ratio concentration-to-final concentration in precipitation processes.

$$f(Y) = Y^r(1 - Y)^m \quad [5]$$

where coefficients r and m are constants. Jena *et al.* reported the best fit values of r, m, k_0, and E_A for several phase transformations in the precipitation sequences of the AlCuMg family, namely GPBZ precipitation, GPZ dissolution, dissolution of GPBZ-dislocation complexes, and S′ precipitation. A good fit to a JMAK model with $n = 1.0$ was also obtained for the latter transformation. Though the model by Jena combines kinetics and thermodynamics considerations, its physical basis is not described. Finally, Yannacopoulos *et al.*[21] calculated the activation energies of the formation and dissolution of GPZ as well as those of formation of other precipitates *via* the Kissinger method. This author used an expression based on chemical reactions obeying an m-order Eyring rate.

Tables I and II summarize the models reported in this section that have been proposed for the reaction rates of the various phase transformations involved in the precipitation sequences of AA 7075 and AA 2024. The values found in the literature for the activation energies of the mentioned phase transformations are also included in these tables.

The purpose of this work is to correlate the viscoelastic response of the studied alloys with the available information on the precipitation path. The test data is presented in Section II. In Section III, a model is described and fitted to experimental data. The results are discussed in Section IV.

Table I. Proposed Models and Activation Energies for Phase Transformations Involved in the Precipitation Sequence of AA 7075*

Process	Model	E_A [eV/atom]	Reference	Observations
GPZ formation	$F = F_f - (F_f - F_i)\exp\left(\frac{-t}{t_C}\right)$ $t_C = t_0 \exp(\frac{E_A}{KT})$ $\frac{dY}{dt} = (1 - Y)^m \exp(\frac{-E_A}{KT})$	0.59 to 0.67 0.35 to 1.08	8 21	commercial AlZnMgCu AlZnMgZr alloy
GPZ dissolution	Eq. [3] and Eq. [2]	1.40 0.78 and 1.27 1.23	22 20 23	AA 7075-T6 AA 7075, 6 months at RT AA 7075-T6
η' formation	Avrami Eq., $n = 2.3$ to 2.8	0.57 to 0.62	21	AlZnMgZr alloy
η' dissolution	—	—	20	not good for kinetics analysis
η formation	—	—	20	not good for kinetics analysis
η dissolution	—	—	15, 20, 23	thermodynamically controlled

*Some information is missing, as not all the transformations have been fully analyzed. In some cases, data from other AlZnMg alloys is presented, when available.

Table II. Proposed Models and Activation Energies for Phase Transformations Involved in the Precipitation Sequence of AA 2024. Some Information is Missing, as Not all the Transformations Have Been Fully Analyzed. In Some Cases, Data from Other AlCuMg Alloys is Presented, When Available

Process	Model	E_A [eV/atom]	Reference	Observations
GPZ/GPBZ formation	Arrhenius-type Eq.	0.54 to 0.66	15	AlCuMg alloy
	Avrami Eq.	0.76 and 0.79	12	AA 2124
GPZ/GPBZ dissolution	Arrhenius-type Eq.	1.28	15	AlCuMg alloy
	Eq. [3] and Eq. [2]	0.82 and 1.31	20	AA 2219-T31 & AA 2219
		1.66	12	AA 2124
θ'' formation	—	1.34	14	AA 2024 & AA 2618
		1.33 and 1.36	12	AA 2124
θ'' dissolution	—	—	—	No references were found
θ' formation	Avrami Eq., $n = 1.1$	1.21	14	AA 2024 & AA 2618
		1.21	20	AA 2219-T31 & AA 2219
		1.18 and 1.33	12	AA 2124
		0.75 and 1.10	24	AlCu alloy
		1.20 and 1.02	25	
		1.25 ± 0.09	26	
θ' dissolution	—	—	20	Not good for kinetics analysis
θ formation	—	—	20	Not good for kinetics analysis
θ dissolution	—	—	15,20,24	Thermodynamically controlled
S′ formation	Arrhenius—type Eq.	1.35	14	AA 2024 and AA 2618
	Eq. [4] and Avrami Eq., $n = 1.0$		15	AlCuMg alloy
S′ dissolution	—	—	15	Thermodynamically controlled
S formation	—	—	—	No references were found
S dissolution	—	—	—	No references were found

II. EXPERIMENTAL

A. *Materials and Methods*

A TA Instruments Q800 dynamic-mechanical analyzer (DMA) (TA Instruments, New Castle, DE) has been used to measure the viscoelastic response of AA 7075-T6 and AA 2024-T3. The DMA is able to apply a mechanical excitation of selected frequency and amplitude under controlled temperature conditions while recording displacements and stiffness. This allows the evaluation and characterization of intrinsic and extrinsic mechanical properties of the material, namely the creep response or the viscoelastic behavior (*e.g.*, the storage modulus, the loss modulus, and the loss tangent) as a function of frequency and temperature. The storage modulus E' is the elastic (real) component of the tensile modulus, which is a measure of the deformation energy stored by the material. The loss modulus E'' is the viscous (complex) component of the tensile modulus, and it accounts for the energy dissipation due to internal friction during relaxation processes.[1] The tested specimens were rectangular plates of 60 mm in length, 8 to 15 mm in width, and 2 mm in thickness. These samples were machine cut from sheet of as-received, commercial AA 7075-T6 and AA 2024-T3. The DMA was configured to sequentially apply dynamic loading with frequencies of 100, 30, 10, 3, and 1 Hz, under isothermal conditions and at different temperatures, from 308 K to 648 K (35 °C to 375 °C) in step increments of 5 K. During the tests, data were isothermally recorded, and aside from other parameters, the storage and loss moduli were computed for each of the frequencies at each temperature step.

B. *Experimental Results on Viscoelastic Response for AA 7075-T6 and AA 2024-T3*

Experimental data of the storage and loss moduli for AA 7075-T6 as a function of temperature for mechanical excitations of frequencies 100, 30, 10, 3, and 1 Hz were already reported.[27] Figure 1 shows the storage modulus for AA 2024-T3 as a function of temperature for mechanical excitations of frequencies 100, 30, 10, 3, and 1 Hz. Qualitatively, the behavior is the same as for AA 7075-T6, and differences in absolute values at RT are within experimental error. As a general trend, the storage modulus decreases initially with temperature for all the studied frequencies. The slope becomes more pronounced at about 413 K to 463 K (140 °C to 190 °C), and an inflexion appears around 473 K to 523 K (200 °C to 250 °C). Finally, there is a local maximum around 523 K to 573 K (250 °C to 300 °C), after which the storage modulus decreases again. For lower frequencies, the maximum is reached at lower temperatures. The storage modulus depends more significantly on frequency at high temperatures, *i.e.*, above 373 K (100 °C), and it is almost insensitive to frequency below this temperature threshold. In addition, at high temperatures, the decrease in the storage modulus at low frequencies is larger than that at higher frequencies; *i.e.*,

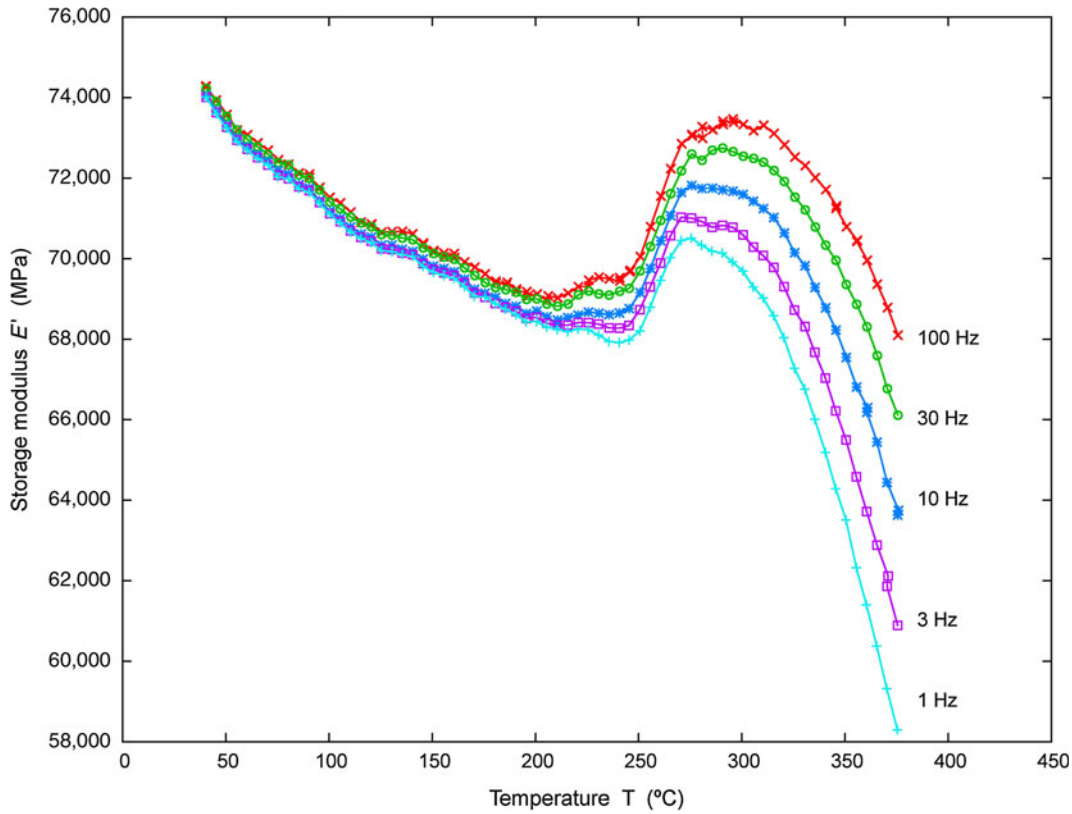

Fig. 1—Storage modulus E' *vs* temperature T obtained by DMA tests on AA 2024-T3 at 100, 30, 10, 3, and 1 Hz, from 308 K to 648 K (35 °C to 375 °C).

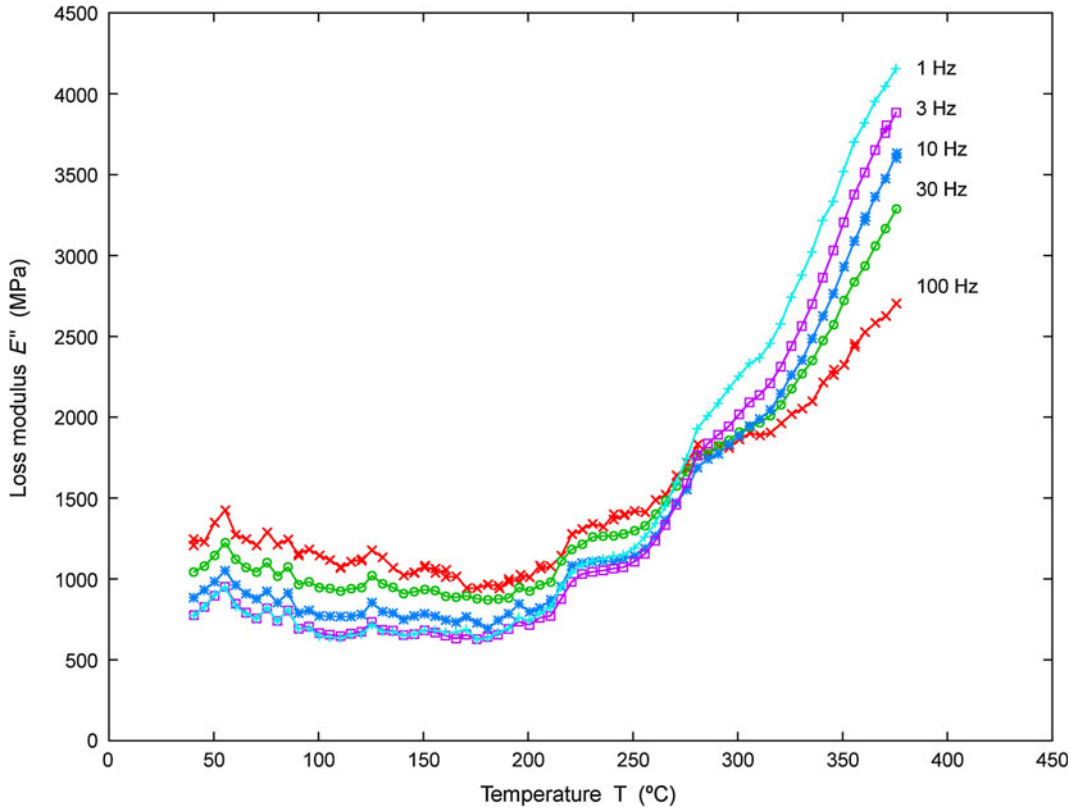

Fig. 2—Loss modulus E'' *vs* temperature T obtained by DMA tests on AA 2024-T3 at 100, 30, 10, 3, and 1 Hz, from 308 K to 648 K (35 °C to 375 °C).

the material seems stiffer at higher frequencies, as expected.

Figure 2 shows the behavior of the loss modulus for AA 2024-T3, also qualitatively similar to that for AA 7075-T6. Particularly, after exhibiting no significant changes at low temperatures for all frequencies, it starts to rise at about 473 K (200 °C), with decreasing slopes as the mechanical excitation frequency is increased. For most of the tests, the loss modulus increases with temperature monotonically; *i.e.*, no peak is observed in the studied temperature range for almost all cases. Finally, it is noteworthy that at higher temperatures (*e.g.*, for AA 7075-T6 above 423 K [150 °C], and for AA 2024-T3 above 523 K [250 °C]) the loss modulus is smaller for higher frequencies of mechanical excitation. This is consistent with the behavior of the storage modulus, as stiffer materials have less energy losses. Conversely, the loss modulus is smaller for lower frequencies at low temperatures. The origin of this unexpected behavior is yet unknown.

III. MODEL

From the DMA test results for AA 7075-T6[27] and AA 2024-T3 (in Section II–B) and research in the literature for aluminum alloys and other materials,[1,28] we can assume that the viscoelastic response of the studied alloys depends on temperature and the frequency of the mechanical excitation, as well on the microstructure and thus the phase transformations. We propose a model for the storage modulus in accordance with this (Section III–A). We also considered modeling the loss modulus (or the internal friction, which exhibits qualitatively the same behavior), but this option was finally disregarded because of the following reasons:

(a) While both moduli contain information about the viscous behavior of the material, the storage modulus contains also information about the elastic behavior.[1]
(b) Maxima observed in the loss modulus (or the internal friction) are related to transformation processes.[28] We observe a monotonic increase of the loss modulus with temperature, due to superposition of peaks corresponding to successive transformations. This is revealed for AA 2024-T3 in Figure 2, where inflexion points due to quasi-local maxima can be identified at 493 K and 573 K (220 °C and 300 °C), coincident with the end of GPZ/GPBZ dissolution and the end of θ'/S′ formation, respectively (Section III–A). The drawback is that the overlapping of successive peaks introduces large noise in any fitting procedure.
(c) We were not able to determine univocally the nature of the relaxation processes developed under heating. Thus, a model of the loss modulus would depend on nondefined parameters related to frictional energy loss.

A. *Modeling of the Storage Modulus*

We propose an analytical model for the storage modulus E' as a function of temperature T, the frequency of the dynamic loading f, GPZ concentration denoted as C_1, and the concentration of the corresponding secondary phases (η' in AA 7075-T6 and θ'/S′ in AA 2024-T3) denoted as C_2:

$$E'(f,T) = E'_{RT}(f) + E'_0(f)(T - RT) + E'_1(f)C_1(T) + E'_2(f)C_2(T) \quad [6]$$

where E'_{RT} is the storage modulus at RT of a GPZ-free alloy, E'_0 accounts for the storage modulus linear decrease with temperature in absence of transformations, E'_1 reflects the contribution of GPZ/GPBZ, and E'_2 accounts for the contribution of the secondary precipitates.**

**For the sake of model simplicity, for AA 7075, the third term on the r.h.s. of Eq. [6] accounts for the joint effect of GPZ I and GPZ II. For AA 2024, this term accounts for the joint effect of GPZ I, GPZ II, and GPBZ, and the last term accounts for the joint effect of θ' and S′. This trade solution stems from the yet unknown isolated effect of each one of these particular phases on the storage modulus, to the author's knowledge. Thus, for AA 2024, C_1 stands for the combined GPZ I, GPZ II, plus GPBZ concentration, and C_2 accounts for the combined θ' plus S′ concentration.

The linear decrease of the storage modulus with temperature reflects the well-known temperature dependence of the elastic stiffness constants of metals. Particularly, according to the literature,[29–32] the static elastic (or Young's) moduli of pure Al and AA 2024 decreases linearly with temperature in the test temperature range. Deviations from this linear behavior were reported close to the absolute zero and above 573 K (300 °C), far from the region of applicability of this model. Also, Wolfenden and Wolla[33] observed a highly linear decrease of the dynamic elastic modulus with temperature from RT to 748 K (475 °C), measured at a high frequency (80 kHz), for pure Al and for AA 6061 reinforced with alumina (Al_2O_3). Finally, the dynamic elastic modulus that we obtained with the DMA for AA 2024-T3 and pure Al compare well to the static and dynamic elastic modulus data available in the literature (Figure 3). Thereby, for modeling purposes, we assumed that the storage moduli of AA 7075 and AA 2024 also decrease linearly with temperature.

Concerning the influence of GPZ/GPBZ on the storage modulus, we took into account that for AA 7075-T6, the microstructure at RT consists primarily of GPZ[22,23] and some η' precipitates,[11,22,23] while for AA 2024-T3, the microstructure at RT consists of GPZ/GPBZ, and the presence of secondary precipitates is negligible.[34] We assumed that the only transformation occurring below 493 K (220 °C) for both alloys was GPZ/GPBZ dissolution, based on TEM and DSC studies in the literature (Tables III and IV). Although

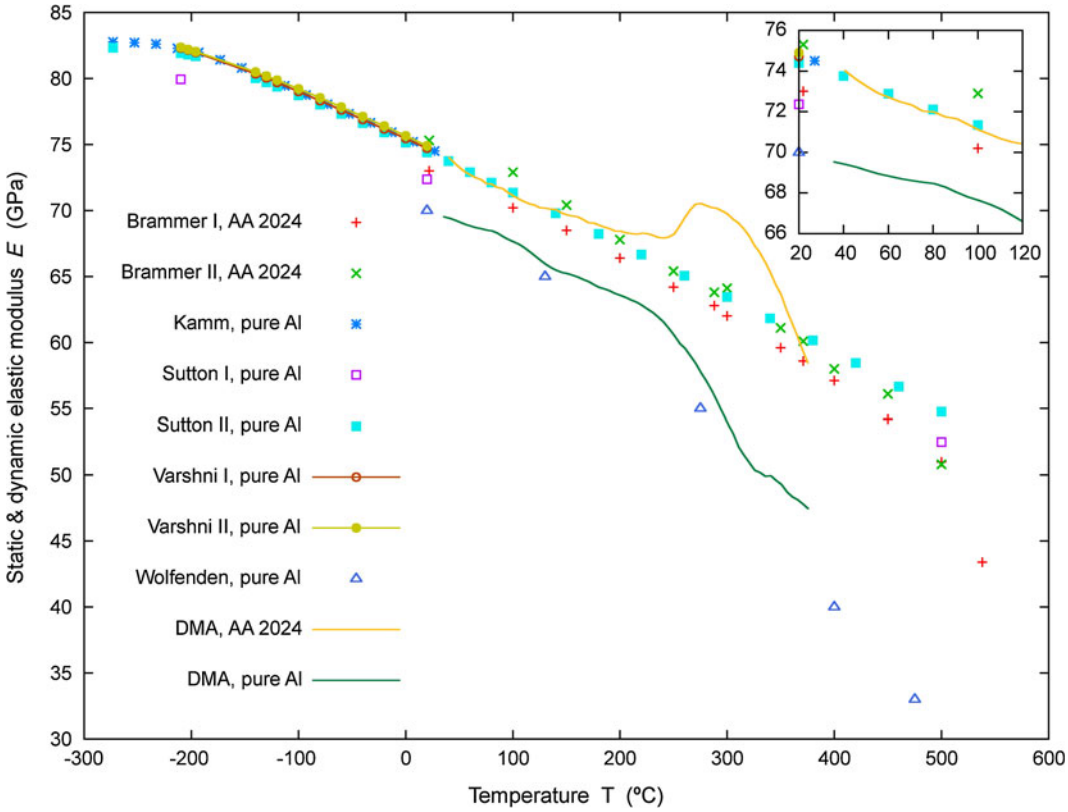

Fig. 3—Elastic modulus E (static and dynamic) *vs* temperature T. Static elastic modulus data were obtained from the literature for pure Al[29,30,32] and for AA 2024.[31] Dynamic elastic modulus was obtained from the literature for pure Al at 80 kHz[33] and from DMA tests for AA 2024-T3 and pure Al at 1 Hz. All data are experimental, except those from Varshni's models.[32].

Table III. Characteristic Temperatures for Transformations in the Aging Sequence of AlZnMg Alloys

Transformation	Temperature* (K)	Heating Rate* (K/min)	Reference
GPZ formation	at 298		10, 35, 36
	at 350	**5**, 10, 20, 40, 60	37
	from 298 to 343	10	11
GPZ dissolution	above 373		36
	at 463	10	11, 38
	at 473	15	39
	from 373 to 423	**1**, 5, 10, 20	20
	from 373 to 490	5, 10, 20	23
	from 403 to 492	10, 15	22
η' formation	at 462	**5**, 10, 20, 40, 60	37
	at 503	10	11, 38
	at 523	3–20	21
	from 373 to 473		8
	from 490 to 544	5, 10, 20	23
	from 492 to 579	10, 15	22
η' dissolution	at 530	10	11

*The temperatures in this table may correspond to peak or start-to-end temperatures obtained after DSC scans, and thus, they may vary with particle size and/or heating rate. When data for several heating rates were available, priority was given to data for the closest heating rate to that we used for the DMA tests, *i.e.*, 1 K/min. When known, the heating rate corresponding to the presented data appears in bold letters.

Table IV. Characteristic Temperatures for Transformations in the Aging Sequence of AlCuMg Alloys

Transformation	Temperature* (K)	Heating Rate* (K/min)	Reference
GPZ/GPBZ formation	at 298	in general, 20	40
	at 298 and 347	0.5, **2**, 5, 20, 40	24
	at 298 and 348–353	20	3
	at 348	**5**, 10, 15, 20	15
	at 353	10	41
	at 363	2, 5, 10, 20, 30, 50	14
GPZ/GPBZ dissolution	at 393	20	3
	at 473	**5**, 10, 15, 20	15
	at 473	10	41
	from 373 to 443	**1**, 5, 10, 20	20
	from 393 to 553	in general, 20	40
	from 410 to 520		42
	from 413 to 513	0.5, **2**, 5, 20, 40	24
	from 423 to 523	10	43
	from 423 to 523	20	44
	from 443 to 497	2, 5, 10, 20, 30, 50	14
	from 460 to 570		42
θ' formation	at 559	2, 5, 10, 20, 30, 50	14
	at 586	0.5, **2**, 5, 20, 40	24
	from 473 to 543	**1**, 5, 10, 20	20
θ' dissolution	at 663	0.5, 2, **5**, 20, 40	24
	from 573 to 823	**1**, 5, 10, 20	20
S′ formation	at 543	**5**, 10, 15, 20	15
	at 559	2, 5, 10, 20, 30, 50	14
	at 573	10	41
	from 393 to 553	in general, 20	40
	from 523 to 623	10	43
S′ dissolution	above 623	in general, 20	40
	at 638	**5**, 10, 15, 20	15

*The temperatures in this table may correspond to peak or start-to-end temperatures obtained after DSC scans, and thus, they may vary with particle size and/or heating rate. When data for several heating rates were available, priority was given to data for the closest heating rate to that we used for the DMA tests, *i.e.*, 1 K/min. When known, the heating rate corresponding to the presented data appears in bold letters.

GPZ formation in AA 7075 and GPZ/GPBZ formation in AA 2024 are possible below 493 K (220 °C), we assumed that these precipitation processes were complete prior to testing, and thus, no further GPZ/GPBZ formation took place during the DMA tests. This is based on the particular tempers of the alloys under

investigation and the fact that both had aged at RT for extended periods of time.[†]

[†]For instance, GPZ precipitation for an AlCuMg alloy is completed after 500 minutes of natural aging at RT,[3] and GPZ I in AlZnMg alloys form also by natural aging at RT.[8]

Moreover, we performed repeated DMA tests in some samples from RT to 373 K (100 °C), and we observed that the storage and loss moduli behaved reversibly, showing that no microstructural transformation occurs within that temperature range. Finally, recalling that the mechanical response (and thus, the viscoelastic behavior) of AlZnMg alloys below 493 K (220 °C) is controlled by GPZ decomposition[10] and considering that there is no other explanation in the literature for the change in storage modulus slope observed around 413 K to 463 K (140 °C to 190 °C), we assumed that this effect is caused by GPZ dissolution in AA 7075-T6 and analogously by GPZ/GPBZ dissolution in AA 2024-T3.

The last term of Eq. [6] reflects the effect of secondary precipitates in the storage modulus. The temperatures reported in the literature for the formation of η' in AA 7075 and θ'/S' in AA 2024 (Tables III and IV) are roughly coincidental with the advent of an increase in the storage modulus leading to a local maximum, while the temperatures for η' and θ'/S' dissolution are roughly coincidental with the subsequent decrease (Figure 1). Hence, as intermediate phases usually do play a role in the mechanical properties and there is no other explanation in the literature for this maximum, we assumed that it is caused by η' formation and dissolution for AA 7075-T6 and θ'/S' formation and dissolution for AA 2024-T3.[‡] Nevertheless, dissolution of η' and θ'/S' phases and formation and dissolution of η and θ/S phases are not accounted for by the model because they overlap and develop mainly out of the test temperature range. Summarizing, the validity of the proposed model is limited to the temperature range where the only significant microstructural transformations that take place are GPZ dissolution and secondary precipitation, *i.e.*, from RT to around 573 K (300 °C).

[‡]From now on for AA 2024, we will use the term GPZ to refer simultaneously to GPZ and GPBZ.

B. *Modeling of Transformation Reaction Rates*

For the reaction rate of GPZ dissolution, we considered various models as proposed in the literature. First, we considered the GPZ dissolution a thermally activated process following Arrhenius behavior, as stated by Jena[15,18]; that is,

$$\frac{dC_1}{dt} = -C_1 k_0 \exp\left(-\frac{E_A}{KT}\right) \qquad [7]$$

We considered also a 3-D diffusion controlled rate expression (Eq. [2]) and a first-order diffusion rate expression (Eq. [3]),[20] which we will refer to, respectively, as Pap. I and Pap. II from now on. These three rate equations were all implemented in the nonlinear fitting process and cross checked to ascertain which one provided a better fit to the experimental data.

As per the modeling of the precipitation rate of η' and θ'/S', we used only the Avrami equation. For AA 2024, it is reasonable to use this equation to represent the evolution of the combined θ'/S' concentration since the formation of both phases exhibit similar activation energies and Avrami indexes. Following Papazian's work, the Avrami equation we implemented in our model to obtain the concentration was in the form

$$\left[-\ln\left(1-\frac{C_2}{C_{2,\text{final}}}\right)\right]^{1/n} = \frac{k_0 E_A}{K\phi}\int_{\frac{E_A}{KT}}^{\infty}\frac{e^{-x}}{x^2}dx \qquad [8]$$

C. *Integration of the Model*

The numerical integration of the rate equations for GPZ dissolution and secondary precipitates formation was performed inside the least-squares nonlinear fitting of the storage modulus model to experimental data. This procedure was coded MATLAB (The MathWorks Inc., Natick, MA).[45] This procedure allowed us to treat the preexponential coefficients, the activation energies, and the Avrami indexes in these rate equations as fitting parameters, in addition to the four coefficients E'_{RT}, E'_0, E'_1 and E'_2 for each frequency, for a total of $5 + 4z$ fitting parameters (z is the number of frequencies solved simultaneously). For all the simulations reported in this article, five frequencies were analyzed (100, 30, 10, 3, and 1 Hz), for a total of 25 fitting parameters. To avoid local minima in the fitting parameters, we performed partial fittings and checked the convergence of the fitted parameters. Particularly, we fitted our model to data between RT and temperatures ranging from 373 K to 598 K (100 °C to 325 °C), in step increments of 15 K.

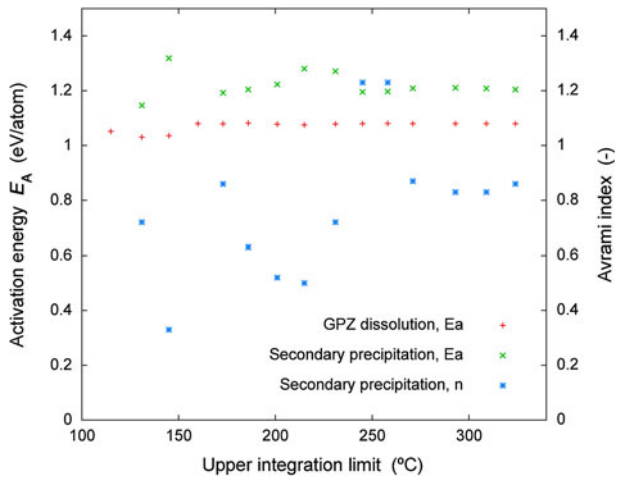

Fig. 4—Activation energies E_A for GPZ dissolution and secondary precipitation, and Avrami index n for secondary precipitation *vs* temperature T of the upper integration limit, for a sequence of simulations covering from 298 K to 373 K (25 °C to 100 °C, RT–100 °C) to 298 K to 598 K (25 °C to 325 °C, RT–325 °C).

Figure 4 shows an example of the evolution of the fitted kinetic parameters resulting from this procedure. As expected, the fitted parameters oscillate when the upper limit of integration is close to 373 K (100 °C) but converge when it approaches 573 K (300 °C), thus confirming the robustness of the procedure and the quality of the fitted parameters.

D. *Results for AA 7075-T6*

The initial values for the fitting parameters as used in the integration of our model were directly taken or estimated from data available in the literature.[3,9,20,21,23,29–33,46,47] Figure 5 shows the computed storage modulus compared with experimental data for a test series on AA 7075-T6 at excitation frequencies of 100, 30, 10, 3, and 1 Hz. Figure 5 shows also the evolution of GPZ and η' concentration with temperature. Both concentration curves exhibit a characteristic sigmoidal shape, which is expected for the second case, as it is typical of the Avrami equation used to model the rate of η' precipitation.

The physical quantities of interest for AA 7075, *i.e.*, the preexponential coefficient and the activation energy of GPZ dissolution when using Jena's and Papazian's rate equations, as well as those of η' formation, together with the Avrami exponent, are listed in Table V. The coefficients E'_0, E'_1, and E'_2 of the storage modulus model are plotted as a function of the excitation frequency in Figure 6.

E. *Results for AA 2024-T3*

As per AA 2024-T3, the initial values for the fitting parameters were also taken or estimated from data available in the literature.[1,3,9,12,15,20,24,29–33,46,47] Figure 7 shows the computed storage modulus compared to the experimental data for a test series on AA 2024-T3 at excitation frequencies of 100, 30, 10, 3, and 1 Hz. Figure 7 shows also the evolution of GPZ and θ'/S' concentration with temperature. Both concentration curves exhibit a characteristic sigmoidal shape, which is again expected for the second case, as it is typical of the Avrami equation used to model the rate of θ'/S' precipitation.

The physical quantities of interest for AA 2024, *i.e.*, the preexponential coefficient and activation energy of GPZ dissolution when using Jena's and Papazian's rate equations, as well as those of θ'/S' formation, together with the Avrami exponent, are listed in Table VI.

The coefficients E'_0, E'_1 and E'_2 of the storage modulus model are plotted as a function of the excitation frequency in Figure 8.

IV. DISCUSSION

The experimental results show that the viscoelastic responses (*i.e.*, the storage and loss moduli) of AA

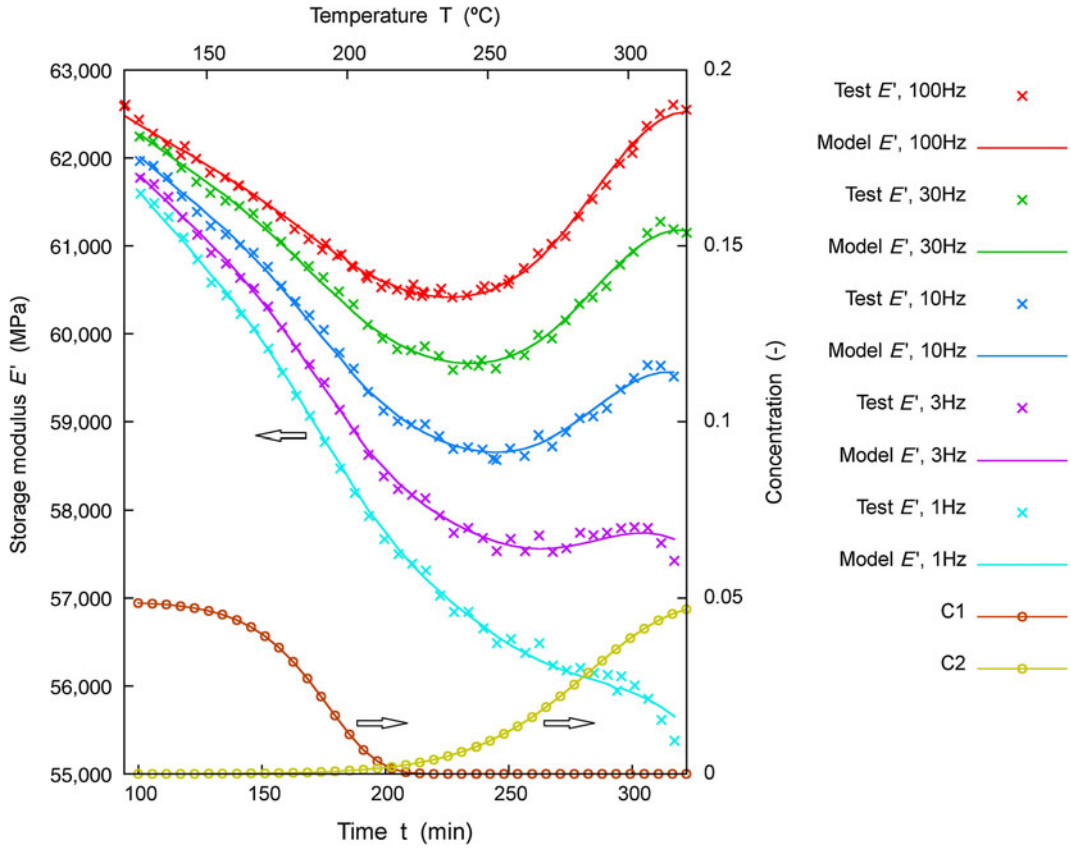

Fig. 5—Experimental and computed storage modulus E' *vs* time t for AA 7075-T6, at excitation frequencies of 100, 30, 10, 3, and 1 Hz, and GPZ concentration C_1 and η' concentration C_2 *vs* temperature T.

Table V. Best-Fit Values Obtained after Integration and Fitting of the Transformation Rate Equations and the Proposed Storage Modulus Model, for AA 7075-T6

Transformation	Kinetic Parameter	Model Used for GPZ Dissolution Reaction Rate		
		Jena	Pap. I	Pap. II
GPZ dissolution	activation energy, E_A	1.21 eV/atom	1.13 eV/atom	1.06 eV/atom
	preexponential coefficient, k_0	1.15×10^{10} s^{-1}	1.38×10^{10} s^{-1}	1.38×10^{10} s^{-1}
η' formation*	activation energy, E_A	1.26 eV/atom	1.26 eV/atom	1.26 eV/atom
	preexponential coefficient, k_0	8.76×10^{9} s^{-1}	8.83×10^{9} s^{-1}	8.38×10^{9} s^{-1}
	Avrami index, n	0.77	0.84	0.76

*The fitting of the Avrami equation parameters varies if the GPZ dissolution rate equation is changed.

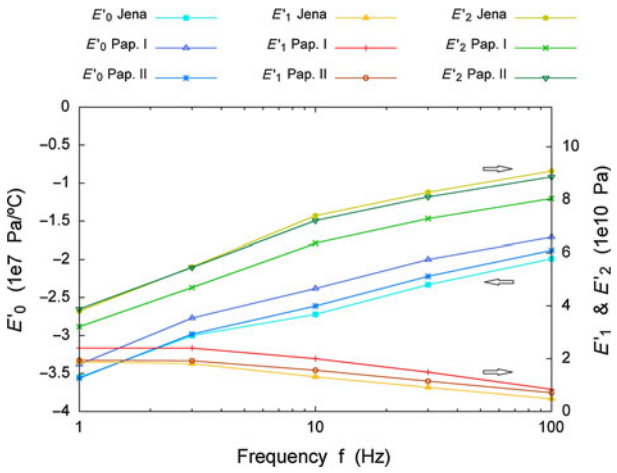

Fig. 6—Coefficients E'_0, E'_1 and E'_2 of the storage modulus model *vs* frequency f for AA 7075-T6.

7075-T6 and AA 2024-T3 are very similar. The initial decrease (as early as at RT) of the storage modulus with temperature for both AA 7075 and AA 2024 is explained by the dependence of the elastic moduli (*i.e.*, the elastic stiffness constants) on temperature, which is a well-known phenomenon for metals, and particularly for aluminum.[29–33] This decrease of the storage modulus has also been observed in AA 6061 and AA 6061-T6.[28] The experimental dynamic elastic moduli of AA 2024-T3 and pure Al at RT compare well to the elastic modulus data available in the literature (Figure 3), as expected since the contribution of the loss modulus is very small and frequency has very little effect at low temperatures. The latter data series exhibits similar slopes with temperature in the vicinity of RT, except from Wolfenden and Wolla's[33] for which the slope is steeper by a factor of 2. The larger decrease of the storage modulus with temperature at low frequencies rather than at high frequencies is typically explained by the Arrhenius-type behavior of the relaxation rate, which means that the mechanical relaxation time diminishes as the temperature increases.[1,48] That is, at low frequencies, the shorter relaxation times cause responses with larger phase lags, which result in a greater decrease of the storage modulus. This explains also why the inflexion and local maximum for higher frequencies are delayed in temperature with respect to lower frequencies. The fact that the viscoelastic behavior becomes more prominent as temperature increases has already been observed in amorphous alloys.[48] In particular, the storage and loss moduli depend more significantly on the excitation frequency at higher temperatures. The results expose also the influence of microstructural transformations on the viscoelastic behavior, in agreement with previous research.[1,28] Particularly, the observed variation in the storage modulus slope at 413 K to 463 K (140 °C to 190 °C), unexplained until now, is ascribed to GPZ dissolution. This result is in good agreement with Macchi *et al.*,[10] who pointed out that the mechanical response of AlZnMg alloys below 493 K (220 °C) is controlled by GPZ decomposition. Furthermore, we ascribe the storage modulus inflexion at 473 K to 523 K (200 °C to 250 °C) and local maximum at 523 K to 573 K (250 °C to 300 °C) to the continuation[§] and completion of η' precipitation for AA 7075, and θ'/S' precipitation for AA 2024, as these transformations take place roughly between 473 K and 573 K (200 °C and 300 °C), and to the author's knowledge, there is no other proposed explanation for these variations. Finally, the decrease in storage modulus after the local maximum may be due to η' (θ'/S') dissolution, again because it occurs roughly in the temperature interval in which the previous transformations typically take place, *i.e.*, at around 573 K (300 °C) and higher temperatures.

[§]The term "continuation" is preferred to "beginning" because some η' precipitates are likely to be already present in AA 7075-T6 at RT.

The model proposed in Eq. [6] fits the experimental data in the prescribed temperature range, *i.e.*, 298 K to 573 K (RT to 300 °C).[§§] Linking the mechanical response to the kinetics of the successive microstructural transformations allows us also to test the proposed models for the process of GPZ decomposition and secondary precipitation. It is noted that the description of GPZ decomposition with Jena's reaction rate (Eq. [7]) leads to the overall best fit for AA 7075, followed closely by the fit obtained when using Eq. [3]. The overall best

[§§]Slight deviations observed in the vicinity of the upper limit (*i.e.*, the storage modulus maximum) are likely due to the advent of secondary precipitates redissolution, which is not represented in our model.

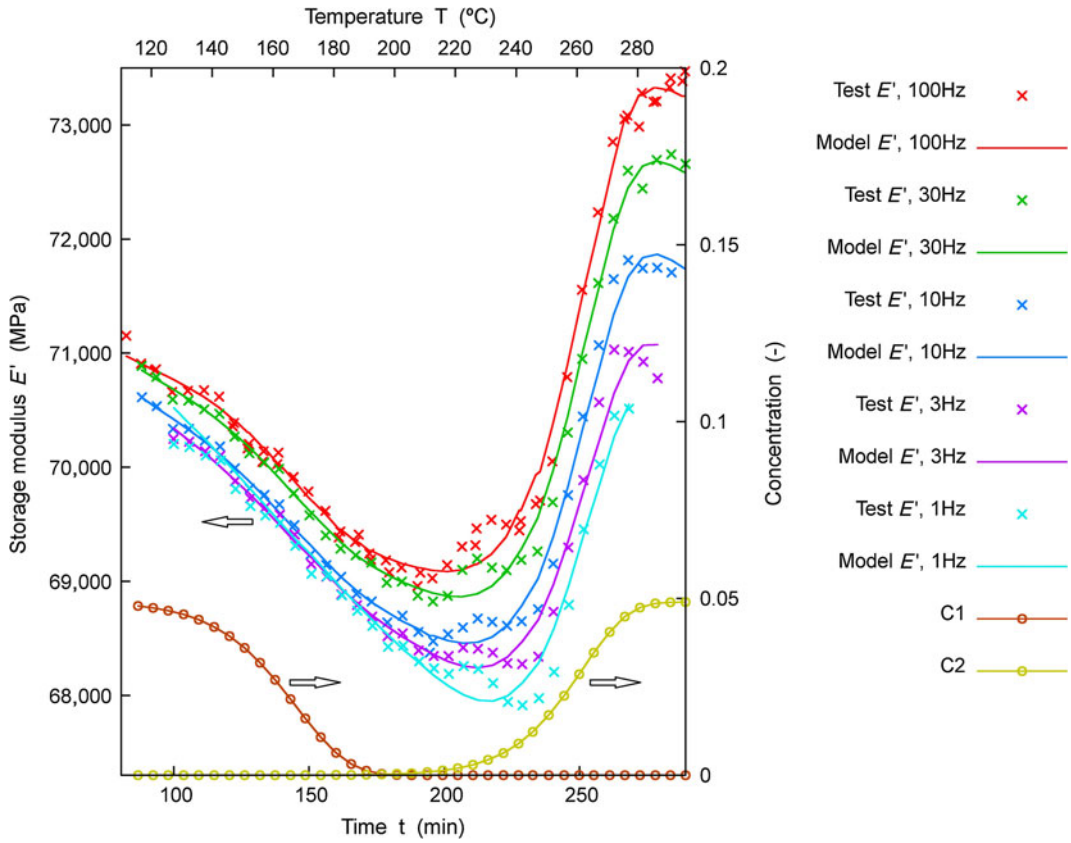

Fig. 7—Experimental and computed storage modulus E' *vs* time t for AA 2024-T3, at excitation frequencies of 100, 30, 10, 3, and 1 Hz, and GPZ concentration C_1 and θ'/S' concentration C_2 *vs* temperature T.

Table VI. Best-Fit Values Obtained after Integration and Fitting of the Transformation Rate Equations and the Proposed Storage Modulus model, for AA 2024-T3

		Model Used for GPZ Dissolution Reaction Rate		
Transformation	Kinetic parameter	Jena	Pap. I	Pap. II
GPZ dissolution	activation energy, E_A	1.18 eV/atom	1.07 eV/atom	0.97 eV/atom
	preexponential coefficient, k_0	4.53×10^{10} s^{-1}	1.00×10^{10} s^{-1}	6.11×10^{9} s^{-1}
η' formation*	activation energy, E_A	1.23 eV/atom	1.23 eV/atom	1.25 eV/atom
	preexponential coefficient, k_0	1.88×10^{10} s^{-1}	1.75×10^{10} s^{-1}	2.75×10^{10} s^{-1}
	Avrami index, n	1.29	1.30	1.30

*The fitting of the Avrami equation parameters varies if the GPZ dissolution rate equation is changed.

fit for AA 2024 is also obtained when using Jena's reaction rate (Eq. [7]), but this time, the goodness of the fit is practically the same for the three models considered.

In regard of GPZ dissolution kinetics for both AA 7075 and AA 2024, the fitted values of the preexponential coefficient and the activation energy are coherent with the values reported in the literature[1,12,15,20,22,23] (Tables I,II,V, and VI). Nevertheless, the activation energy seems to be technique sensitive, as the reported values fall in a broad range (0.82 to 1.66 eV per atom for AA 2024, and 0.78 to 1.40 eV per atom for AA 7075). Papazian[20] affirmed that the activation energy for Cu GPZ dissolution should be close to that for chemical interdiffusion in the AlCu systems, which is around 1.24 to 1.47 eV per atom.[20,49] While the values obtained for AA 2024 using Papazian's rate expressions (Eq. [2] and [3]) are not far from this range, the activation energy obtained when using Jena's rate equation Eq. [7] is the closest (1.18 eV per atom). In any case, it is reasonable to believe that diffusion of Cu in Al plays a key role in GPZ dissolution for AA 2024. For AA 7075, again the result obtained when using Jena's rate equation (1.21 eV per atom) is the closest to most of the values found in the literature. It is noted also that the activation energy of Zn/Mg GPZ dissolution is close to that for migration of Mg and Zn in Al, *i.e.*, around 1.14 to 1.35 and 1.22 eV per atom, respectively.[49] Summarizing, the models proposed by Papazian apparently lead to a slight underestimation of the activation energy for both AA

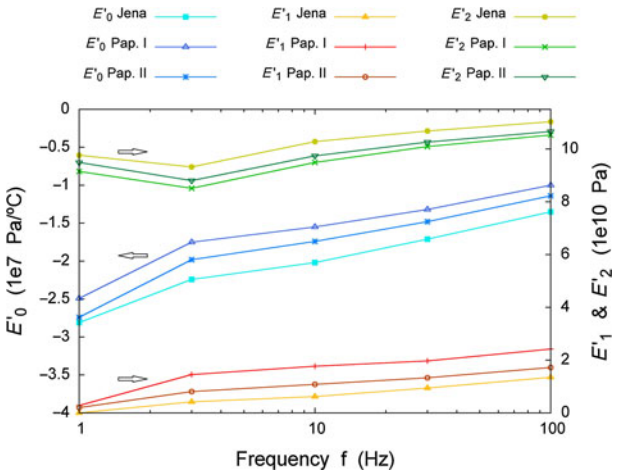

Fig. 8—Coefficients E'_0, E'_1 and E'_2 of the storage modulus model *vs* frequency f for AA 2024-T3.

7075 and AA 2024. Hence, the reaction rate proposed by Jena (Eq. [7]) is the most appropriate to model GPZ dissolution.

As per the kinetics of η' precipitation, there is a noticeable disagreement between the activation energy and Avrami index reported in the literature[21] (Tables I and V) and those obtained in this work. Yannacopoulos *et al.*[21] obtained activation energies of 0.57 to 0.62 eV per atom and Avrami exponents of 2.3 to 2.8, while we obtained 1.26 eV per atom and 0.76 to 0.84, respectively. Avrami exponents around 2.5 may correspond to a 3-D diffusion-controlled transformation with continuous nucleation. The transformation being controlled by diffusion is consistent with the fact that long-range Mg and Zn migration is probably necessary for it to occur, but a continuous nucleation throughout the transformation seems not feasible in this case given that (1) in tests at constant heating rate, constant nucleation rates generally do not occur[19]; and (2) precipitation of η' occurs *via* nucleation from, or at, sites of GPZ,[8,10,50] which are already abundant in the T6 temper at RT.[23] Therefore, site-saturated nucleation is highly probable, as it occurs for other alloys.[19] Conversely, Avrami indexes equal to or slightly smaller than 1.00 (like those that we obtained from our model) are typical of site-saturated 2-D diffusion-controlled precipitation, which agrees also with the plate shape reported for η'.[9,51] In addition, the activation energy for η' precipitation should be higher than that for GPZ dissolution because of the higher temperatures necessary for it to occur. Consequently, our results for the kinetic parameters are more consistent than those reported by Yannacopoulos *et al.*

Regarding θ'/S' precipitation, there is a good agreement between the activation energies reported here and those available in the literature[12,14,20,24] (Tables II and VI). Nevertheless, there is a large dispersion in the latter values, as in previous cases. Starink and Vanmourik[24] presented several explanations for the dispersion in measured activation energies for θ' formation, and they observed that in general, the values were lower than that for Cu diffusion in Al and self-diffusion in Al, which is also the case for our results. The computed preexponential coefficients are larger by approximately an order of magnitude. Finally, the computed Avrami indexes are slightly larger than those in the literature[15,20] but fall in the same range, *i.e.*, 1.0 to 1.5, which is commonly associated to site-saturated 2-D or 3-D diffusion-controlled transformations. This is coherent with θ'/S' precipitation because, for instance, (1) the θ' phase is plate shaped[20,24] and (2) it nucleates on the faces of GPZ II[16]; therefore, site-saturated nucleation is again likely since numerous nuclei (*i.e.*, GPZ) are already present at RT.

As per the behavior of the model coefficients, it is first observed that varying the excitation frequency has no significant effect on E'_{RT}, as it is expected, since the viscoelastic response (and particularly, the storage modulus) dependence on frequency weakens as temperature decreases. On the contrary, the coefficient E'_0, which represents the rate of storage modulus loss with temperature, increases significantly with frequency (*i.e.*, becomes less negative) both for AA 7075 and AA 2024. This finding is coherent with the expected lower decrease of the storage modulus with temperature at high frequencies as compared to low frequencies. The values that we obtained for E'_0 are smaller (but of the same order of magnitude) than that reported by Wolfenden (–80 MPa $°C^{-1}$) for pure Al at 80 kHz.[33]

The coefficient E'_1 has a different behavior in the two alloys analyzed. All coefficients show a slightly larger dispersion in AA 2024 compared to AA 7075, for the different models considered, and the values of all coefficients at 1 Hz for AA 2024 do not seem to be very reliable, as they clearly seem not to follow the trends. These facts may be related to the higher complexity of the precipitation path of AA 2024 and to the different kinetics observed in both alloys. That is, the Avrami index of the secondary precipitation in AA 7075 is much smaller than in AA 2024, and thus, the secondary precipitation process is slower. This allows a much better determination of the coefficient E'_2 and then reduces the uncertainty in E'_1. Summarizing, the behavior of both coefficients is more consistent in AA 7075. There, E'_1 shows a slight decrease with frequency, as corresponds to a redissolution process, while E'_2 increases noticeably with frequency, as expected in a precipitation process. This increase in E'_2 is also consistent with the behavior of the loss modulus shown in Figure 2, where it can be seen that dissipation effects decrease as frequency increases in the temperature range corresponding to secondary precipitation; *i.e.*, the material appears stiffer at higher frequencies.[1] Nonetheless, the dispersion in the coefficients for AA 2024 does not affect the values of the fitted kinetic parameters, although it appears that they are average values corresponding to the two simultaneous redissolution processes ant the two subsequent precipitation processes, due to the two parallel aging sequences. Unfortunately, the accuracy of the experimental data does not allow us to fit a more detailed redissolution/precipitation kinetic model for AA 2024. Finally, it is observed that for both alloys, the values of the coefficient E'_2 are higher than those of E'_1, which means that secondary precipitates have a more important effect on stiffness per unit concentration than GPZ.

V. CONCLUSIONS

The viscoelastic response of AA 7075-T6 and AA 2024-T3 depends on temperature, the frequency of the mechanical excitation, and the microstructure, and these values are qualitatively very similar. The initial decrease of storage modulus is explained by the dependence of the elastic moduli on temperature. The larger decrease of storage modulus with temperature for lower frequencies and the shift to higher temperatures of the inflexion and local maximum as frequency increases show an Arrhenius-type behavior of the relaxation rate, denoting that the mechanical relaxation time diminishes as temperature increases. Also, the storage and loss moduli depend more significantly on the excitation frequency at higher temperatures. The observed variation in the storage modulus slope at 413 K to 463 K (140 °C to 190 °C) is ascribed to GPZ dissolution, while the storage modulus inflexion at 473 K to 523 K (200 °C to 250 °C) and local maximum at 523 K to 573 K (250 °C to 300 °C) are ascribed to the continuation[§] and completion of η' precipitation in the case of AA 7075, and θ'/S' precipitation in the case of AA 2024. Finally, the decrease in storage modulus after the local maximum may be due to η' (θ'/S') dissolution.

Beyond the qualitative description, a theoretical model allowed us to relate these microstructural transformations to the dynamic-mechanical properties of the alloys. The general agreement of the kinetic parameters obtained from this model to data available in the literature confirms the validity of the approximation. Thereby, it confirms also that the dynamic-mechanical analysis is an adequate tool for studying the material microstructure and the kinetics of such phase transformations. It is of particular interest to note that contrary to DSC analysis, the dynamic-mechanical response is independent of the total enthalpy change of the transformation, thus allowing the analysis of microstructural transformations involving minority phases.

ACKNOWLEDGMENTS

This work was supported by the MICINN Grant MAT2010-14907 and Generalitat de Catalunya Grant 2009SGR01251.

REFERENCES

1. A.S. Nowick and B.S. Berry: *Anelastic Relaxation in Crystalline Solids*, Academic Press, New York, NY, 1972.
2. Y.M. Soifer, N.P. Kobelev, L.G. Brodova, A.N. Mannkhin, E. Korin, and L. Soifer: *Nanostruct. Mater.*, 1999, vol. 12, pp. 875–78.
3. S. Abis, M. Massazza, P. Mengucci, and G. Riontino: *Scripta Mater.*, 2001, vol. 45, pp. 685–91.
4. G. Bierwagen: *J. Coat. Technol.*, 2001, vol. 73, pp. 45–52.
5. A.J. Vreugdenhil, V.N. Balbyshev, and M.S. Donley: *J. Coat. Technol.*, 2001, vol. 73, pp. 35–43.
6. R.M. Chlistovsky, P.J. Heffernan, and D.L. DuQuesnay: *Int. J. Fatigue*, 2007, vol. 29, pp. 1941–49.
7. E.A. Starke and J.T. Staley: *Prog. Aerosp. Sci.*, 1996, vol. 32, pp. 131–72.
8. R. Ferragut, A. Somoza, and A. Dupasquier: *J. Phys. Condens. Matter*, 1996, vol. 8, pp. 8945–52.
9. T. Engdahl, V. Hansen, P.J. Warren, and K. Stiller: *Mater. Sci. Eng. A-Struct. Mater. Prop. Microstruct. Process.*, 2002, vol. 327, pp. 59–64.
10. C.E. Macchi, A. Somoza, A. Dupasquier, and I.J. Polmear: *Acta Mater.*, 2003, vol. 51, pp. 5151–58.
11. F. Viana, A.M.P. Pinto, H.M.C. Santos, and A.B. Lopes: *J. Mater. Process. Technol.*, 1999, vol. 93, pp. 54–59.
12. G.W. Smith: *Thermochim. Acta*, 1998, vol. 317, pp. 7–23.
13. S. Abis, P. Mengucci, and G. Riontino: *Mater. Sci. Eng. A-Struct. Mater. Prop. Microstruct. Process.*, 1996, vol. 214, pp. 153–60.
14. C. Badini, F. Marino, and E. Verne: *Mater. Sci. Eng. A-Struct. Mater. Prop. Microstruct. Process.*, 1995, vol. 191, pp. 185–91.
15. A.K. Jena, A.K. Gupta, and M.C. Chatuverdi: *Acta Metall.*, 1989, vol. 37, pp. 885–95.
16. T.J. Konno, M. Kawasaki, and K. Hiraga: *J. Electron Microsc.*, 2001, vol. 50, pp. 105–11.
17. J.I. Gersten and F.W. Smith: *The Physics and Chemistry of Materials*, 1st ed., Wiley, New York, NY, 2001, pp. 757–67.
18. J.W. Christian: *The Theory of Transformations in Metals and Alloys*, 3rd ed., Pergamon, Oxford, U.K., 2002, pp. 532–46.
19. M.J. Starink and A.M. Zahra: *Thermochim. Acta*, 1997, vol. 292, pp. 159–68.
20. J.M. Papazian: *Metall. Trans. A*, 1982, vol. 13A, pp. 761–69.
21. S. Yannacopoulos, S.O. Kasap, A. Hedayat, and A. Verma: *Can. Metall. Q.*, 1994, vol. 33, pp. 51–60.
22. U. Batra and S.R. Prabhakar: *Trans. Indian Inst. Met.*, 1995, vol. 48, pp. 55–61.
23. E.S. Tankins and W.E. Frazier: *Mater. Perform.*, 1987, vol. 26, pp. 37–44.
24. M.J. Starink and P. Vanmourik: *Mater. Sci. Eng. A-Struct. Mater. Prop. Microstruct. Process.*, 1992, vol. 156, pp. 183–94.
25. H.I. Aaronson and C. Laird: *Trans. TMS-AIME*, 1968, vol. 242, p. 1437.
26. Y.H. Chen and R.D. Doherty: *Scripta Metall.*, 1977, vol. 11, pp. 725–29.
27. J.I. Rojas, A. Aguiar, and D. Crespo: *Phys. Status Solidi C*, 2011, vol. 8, pp. 3111–14.
28. T. Das, S. Bandyopadhyay, and S. Blairs: *J. Mater. Sci.*, 1994, vol. 29, pp. 5680–88.
29. P.M. Sutton: *Phys. Rev.*, 1953, vol. 91, pp. 816–21.
30. G.N. Kamm and G.A. Alers: *J. Appl. Phys.*, 1964, vol. 35, pp. 327–30.
31. JA Brammer and CM Percival: *Exp. Mech.*, 1970, vol. 10, p. 245.
32. Y.P. Varshni: *Phys. Rev. B*, 1970, vol. 2, pp. 3952–58.
33. A. Wolfenden and J.M. Wolla: *J. Mater. Sci.*, 1989, vol. 24, pp. 3205–12.
34. T. Ozawa: *Thermochim. Acta*, 1992, vol. 203, pp. 159–65.
35. R. Graf, I.J. Polmear, and G. Thomas: *J. Inst. Met.*, 1958, vol. 86, pp. 535–38.
36. V. Hansen, K. Stiller, and G. Waterloo: *Mater. Sci. Forum*, 2002, vols. 396–402, pp. 815–20.
37. E. Salamci: *Mater. Sci. Technol.*, 2004, vol. 20, pp. 859–63.
38. J.M. Papazian: *Mater. Sci. Eng.*, 1986, vol. 79, pp. 97–104.
39. J.M. Badia, J.M. Antoranz, and P. Tarin: *Boletín Sociedad Española Cerámica Vidrio*, 2004, vol. 43, pp. 224–28.
40. A. Charai, T. Walther, and C. Alfonso: *Acta Mater.*, 2000, vol. 48, pp. 2751–64.
41. H.C. Shih, N.J. Ho, and J.C. Huang: *Metall. Mater. Trans. A*, 1996, vol. 27A, pp. 2479–94.
42. E.J. Mittemeijer: *J. Mater. Sci.*, 1992, vol. 27, pp. 3977–87.
43. V. Dixit, R.S. Mishra, R.J. Lederich, and R. Talwar: *Sci. Technol. Weld. Joi.*, 2009, vol. 14, pp. 346–55.
44. E. Hersent, J.H. Driver, and D. Piot: *Scripta Mater.*, 2010, vol. 62, pp. 455–57.
45. MATLAB: The MathWorks Inc., R2010b, Natick, MA, 2010.
46. J.K. Park and A.J. Ardell: *Metall. Trans. A*, 1983, vol. 14A, pp. 1957–65.
47. M.M. Sharma, M.F. Amateaub, and T.J. Eden: *J. Alloy. Compd.*, 2006, vol. 416, pp. 135–42.
48. H.T. Jeong, E. Fleury, W.T. Kim, D.H. Kim, and K. Hono: *J. Phys. Soc. Jpn*, 2004, vol. 73, pp. 3192–97.

49. Y. Du, Y.A. Chang, B.Y. Huang, W.P. Gong, Z.P. Jin, H.H. Xu, Z.H. Yuan, Y. Liu, Y.H. He, and F.Y. Xie: *Mater. Sci. Eng. A-Struct. Mater. Prop. Microstruct. Process.*, 2003, vol. 363, pp. 140–51.
50. S.K. Maloney, K. Hono, I.J. Polmear, and S.P. Ringer: *Micron*, 2001, vol. 32, pp. 741–47.
51. M. de Sanctis: *Mater. Sci. Eng. A-Struct. Mater. Prop. Microstruct. Process.*, 1991, vol. 141, pp. 103–21.